Multimedia Photogrammetry for Automated 3D Monitoring in Archaeological Waterlogged Wood Conservation

Robin Rofallski[1], Amandine Colson[2], Thomas Luhmann[1]

[1] Institute for Applied Photogrammetry and Geoinformatics, Jade University of Applied Sciences, Oldenburg, Germany
(robin.rofallski, thomas.luhmann)@jade-hs.de
[2] Denkmal3D, Vechta, Germany - a.colson@denkmal3.de

Keywords: Multimedia Photogrammetry, Wood conservation, Automation, Scale definition

Abstract

This study addresses the challenges inherent in preserving archaeological waterlogged wood, which is prone to deformation and decay if not stabilized immediately after recovery. Conventional preservation methods, such as impregnation with polyethylene glycol (PEG) solutions, often result in undesirable dimensional changes. To obtain exact spatio-temporal information on the deformations during the conservation process, a photogrammetric monitoring system, utilizing a stereo camera facing from air into the liquid, attached to an automated biaxial measurement unit is proposed. Special target heads were developed and attached to the wood to provide deformation points. Refraction correction was applied to the imaging model by ray tracing, and indirect flat lighting was used to mitigate turbidity. The system observed logs from a wooden track from the first century, subject to conservation. Subject of investigation were the influence of refraction negligence and scale definition in a bundle geometry, similar to bathymetric aerial setups. Results show that refraction correction is imperative for good results. Furthermore, scale definition with highly accurately determined scale bars and inclusion of relative orientation constraints provide further accuracy improvements.

1. Introduction

Archaeological waterlogged wood is very challenging and must be preserved immediately after recovery to prevent deformation and decay (Broda and Hill, 2021). However, the usual method of stabilization, an impregnation of bulking agent (polyethylene glycol, PEG) in a water solution, often brings undesirable three-dimensional changes. Given the high costs and environmental impact associated to conventional preservation methods, innovative and tailor-made solutions are required.

The main issue with archaeological waterlogged wood is an uncontrolled drying of the wooden material, which leads to irreversible shrinkage and deformations. Depending on the choices of the conservation method (which bulking agent), its concentration in the wood and the drying approach, problems can occur at different phases. This may include an overall deformation or rotation of the timbers just as local degradation, such as surface cracks. Each archaeological context is unique in terms of geological settings, the nature of the sediment and time spent underground which may differ extremely. Additionally, every wooden species has certain characteristics and degradation states which can vary tremendously caused by fungi, bacteria, contact with air/water over hundreds or thousands of years. Hence, the number of parameters influencing the success of the conservation procedure is large, complicating possible optimization.

Observing geometrical changes of waterlogged wood is a challenging task for a variety of reasons but is currently the only existing approach. Three parameters are established to assess the degradation state and the success of a conservation treatment: the water content (U_{max}), the conventional density (R) and the Anti-Shrinkage Efficiency (ASE) (Björdal, 2000; Jensen and Gregory, 2006). Nevertheless, these parameters have shown their limitations and proven not to be always reliable (Giachi et al., 2010), calling for research. The research project OptiKons, “An optimized conservation of waterlogged archaeological wood with the support of 3D monitoring” aims to develop a monitoring protocol using photogrammetry. Timbers from the wooden track PR 6, Aschener Bog, Lower-Saxony, Germany (Colson et al., 2023), dated from the first century BC are used as the case study.

To develop a monitoring approach using optical technologies, several challenges need to be overcome. As a matter of fact, the surface does not provide rich texture, complicating the use of Structure-from-Motion (SfM) techniques, relying on identifiable features on the object. The wood itself must be handled with care, respecting conservation ethics and applying commercial adhesives on the surface is not possible (Viñas, 2002). Next, the conservation liquid surrounding the wood during impregnation, will over the course of the treatment pose several optical interferences on images observing the wood. This includes reflections on the surface, chromatic aberration, and refraction at interface transitions (i.e. from air to water). However, optical methods provide a large amount of detail to observe the given objects, including color information, high resolution and accuracy, if calibrated accordingly. Thus, we rely on a photogrammetric approach to monitor the waterlogged wood in the conservation liquid during impregnation.

A stereo camera system was attached to an automated biaxial unit, enabling automatic and repeatable movement over the logs to acquire imagery. The system was based on timing belts moving on the rim of a conservation tank of 6 $\times$ 1.5 m. Given the refraction and other challenges that arise from a multimedia environment, we imposed refraction correction on the imaging model. Additionally, the scene was illuminated by submerged indirect flat lighting for turbidity mitigation and ambient lighting was excluded by measuring at night.

In this contribution, we show the potential of an automated photogrammetric monitoring system that runs on a low-cost and light-weight Raspberry Pi 5 and outsources image processing, bundle adjustment and analysis. Hence, automated processing with high computing capabilities could be performed without the need for expensive hardware on premises. This also kept the system compact and able to run on a 24V LiFePo4 battery with limited capacity. Furthermore, we focused on the errors arising with self-calibration from neglecting refraction correction in this multimedia environment against the correct modeling with a performant ray tracing implementation.

2. Related Work

Metrology technologies have been applied very rarely on moveable cultural heritage to detect deformation (Colson, 2024). A few initiatives exist applied on paintings, tapestries, and some on wood. Concerning historical wood, found in dry condition, usually no relevant deformation is expected and hence not a of interest for geometric monitoring. Photogrammetric techniques have been applied for the monitoring of Westminster Retable, a historical painted wooden panel from the 13th century during conservation (Robson et al., 2004). Employing multi-image photogrammetry and strict error propagation, a single-point accuracy of $20\,\mu\mathrm{m}$ could be achieved. Laser triangulation sensors showed the effect of heating during winter on a wooden altarpiece in Rocca Pietore, Italy. The measurements were conducted punctually with micrometer precision (Bratasz and Kozłowski, 2005). Stelzner et al. (2022) conducted computer tomography and structured light scanning on small samples before and after treatment on archaeological wood.

Conserved archaeological wood was monitored in larger structures in museum context, e.g. archaeological ships and boats, such as the Vasa (van Dijk et al., 2016), Bremen Cog (Hastedt et al., 2019; Colson et al., 2022) or the Oseberg Ship (Hauer et al., 2022). So far only five initiatives exist of deformation monitoring of archaeological ships worldwide. But all of them contributed to prove the relevance of geometrical changes over time even beyond conservation, which means that conservation treatments need to be optimized.

For high accuracy, photogrammetric targets are used to provide precise and repeatable deformation points on the object to achieve submillimeter accuracy on a scale of 10 meters and beyond. However, during impregnation and drying, no geometric monitoring had been performed up to this point. The project OptiKons, which this study resulted from, aims to fill this gap and use optical 3D metrology to detect the moment when archaeological waterlogged wood deforms, both underwater and in the air, in order to enable early and adapted conservative measures.

The physics of describing refraction are well-known through Snell’s law. Implementations for multimedia photogrammetry exist, e.g. by Kotowski (1988) who included a strict model to the bundle adjustment. This approach was taken on by Mulsow (2010) and other works of the author to be employed in a universal approach. In the last decade, the computer vision community has caught up on the subject, providing models with computational efficiency as a priority (e.g. Treibitz et al., 2012; Jordt-Sedlazeck and Koch, 2012; Agrawal et al., 2012). Rofallski and Luhmann (2022) provided an efficient optimization to the work of Mulsow and Maas (2014), enabling bundle adjustment in almost real-time for monocular setups with bundle-invariant interfaces. This contribution is focused on applying this model to a stereo setup with a single object-invariant flat interface, i.e. the liquid surface.

3. System setup and methodology

A monitoring system, regardless of the observable, depends on a high degree of repeatability of measurements and a sufficient temporal resolution to obtain deformation information. With this application, additional requirements came into place. This included considerations on the used targets, the bundle geometry, scale definition, multimedia effects and automation which are addressed in the following section.

3.1 Measurement targets

The wood provides some texture to an extent that SfM methods may work but cannot be guaranteed to be solvable and, most importantly, be reliable. Due to the high degree of degradation of the woods and general conservation practice, tactile measurements were ruled out. Possible targets can only be minimally invasive and inserted into the material to not unnecessarily destroy any fragile structure. The developed target heads were specifically designed for this task (Figure 1), made of stainless steel. With a small pin of less than $2\,\mathrm{mm}$ in diameter, penetrating the wood’s surface, and a head located in the center of gravity, the original material was damaged to a limited extend. Additionally, the circular targets provided highly accurate ellipse detection. Also, 6DOF for each target head could be obtained to detect unwanted tilting or turning of the head itself. The targets were designed fitting the photogrammetric objectives and respecting conservation ethics.

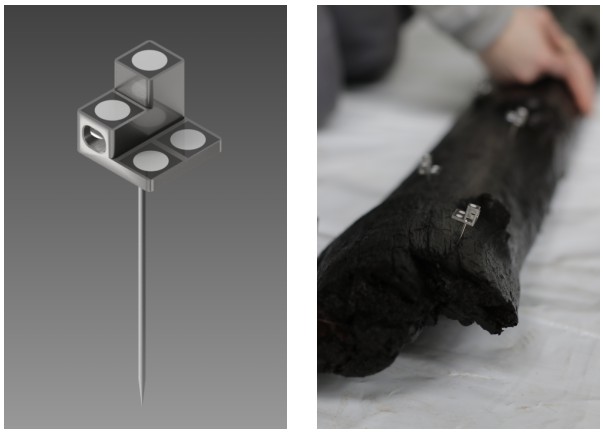

(a) CAD drawing (b) Target head attached to observed wood

Figure 1. Designed target heads for deformation monitoring. The dimensions are $15 \times 15 \times 10\,\mathrm{mm}^3$ for the head with a pin of about $40\,\mathrm{mm}$ in length and $3\,\mathrm{mm}$ diameter.

3.2 Automated biaxial measurement system

Sufficient data on the amount and time frame of deformations in archaeological wood conservation is not available. Hence, both high temporal and spatial resolution are desirable to obtain a first estimate. The given approach is based on a biaxial measurement system which is fully automated to acquire images on a daily basis with submillimeter resolution (Figure 2.) In the longitudinal direction, a timing belt was placed on

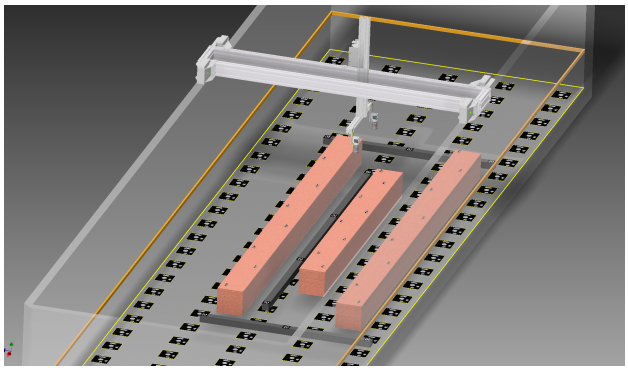

Figure 2. CAD drawing of the setup in the conservation tank with markers on stainless steel bars, marked wood logs and three CFK scale bars spread across the measurement area. The scene is illuminated by LED strips, attached to the tank walls.

the rim of the conservation tank, enabling the system to run on arbitrarily long lengths. In lateral direction, a fixed-length linear unit was employed, tailored to the tank size. Thus, the system could move to any position with a fixed height over ground. Each axis was driven by a stepper motor of sizes NEMA 17 (lateral, x) and NEMA 23 (longitudinal, y). The motor driver board was a Trinamic TMCM3110[1] which enabled a precise step resolution of $0.007°$, translating to a resolution of $1.3\,\mu m$ on the x-axis and $3.5\,\mu m$ on the y-axis. The system was a special development but consisted of standard parts, such as construction profiles, standard motors and machine vision cameras. Material costs are estimated to range around € 6000 - € 8000.

The system carried a photogrammetric stereo system that was attached to a bar, facing downwards. The cameras were placed in air and observed the wood through the liquid. We chose this arrangement over a submerged and housed system because of water bubbles that set quickly and repeatedly on the interface, decreasing image quality substantially. The machine vision cameras (Basler Ace) with $8.5\,mm$ lenses were arranged slightly convergent to obtain a favorable triangulation geometry for the observed points. A low-cost Raspberry Pi 5[2] was the heart of the system and called the routines to the motor control unit. The cameras were connected through USB3 and also triggered through hardware synchronization by the Raspberry's GPIO pins. Data was stored on a server through the internet connection, available on premises.

3.3 Bundle geometry

The three marked logs were placed in the middle of the conservation tank sided by photogrammetric ring coded targets on stainless steel bars. The bars were arranged in five length-spanning lanes which fit up to $30\,cm$ wide logs in between (Figures 2 and 3). The attached deformation points provided points in the depth direction for better determination of focal length and refraction parameters. Additionally, three scale bars made of CFK were placed in the tank for scale definition and evaluation purposes. Both point groups worked as datum points for the following deformation analysis.

The measurement unit meandered over the wood in a height of about $50\,cm$, creating a geometry, similar to an aerial or

[1]https://www.analog.com/en/products/tmcm-3110.html
[2]https://www.raspberrypi.com/products/raspberry-pi-5/

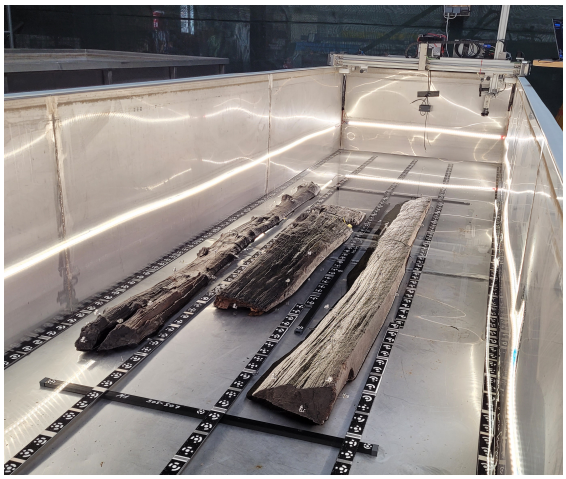

Figure 3. Image of the setup in the conservation tank just before watering the wood

bathymetric triangulation bundle with 80/80 overlap. With a liquid level of about $30\,cm$, the proportion of air to liquid was about $40:60$. Considering the reduced field of view arising from the water refraction, the GSD was at $0.2\,mm$ and each camera captured a footprint of $610\,mm \times 480\,mm$. The system was not capable of varying the acquisition height or rotating around the optical axis. Hence, the resulting bundle geometry is not ideal for self-calibration.

Due to reactions of the conservation agent and the wood, turbidity may increase, impairing passive vision-based approaches. This is highly dependent on the conserved wood and the type of conservation liquid. We therefore also added a laser line for future light-sheet triangulation purposes which should work with higher turbidity than passive image acquisition for bundle adjustment. This however is not part of this study but may be investigated in the future. A sample image pair is shown in Figure 4.

(a) Camera 1 (b) Camera 2

Figure 4. Exemplary stereo images

3.4 Camera calibration and refraction

The liquid surface poses an object-invariant refractive interface that all image rays pass through. Hence, the projection had to be modeled accordingly. We implemented the approach by Rofallski and Luhmann (2022) and extended it for multi-camera systems and an object-invariant interface (Figure 5).

We calculate the refracted image ray and intersection point, according to the ray tracing procedure (Glassner, 1989).

$$\vec{A_{i+1}} = \mu_{rel} \cdot \vec{A_i} + \left(\mu_{rel} \cdot C_i - \sqrt{1 + \mu_{rel}^2 \cdot (C_i^2 - 1)} \right) \cdot \vec{N_i} \quad (1)$$

$\vec{A_i}$ Directional vector in ith medium

$\vec{N_i}$ Normal vector on ith interface

C_i Reversed incidence angle $-cos(\theta_i) = -\vec{N_i} \cdot \vec{A_i}$

μ_{rel} Relative refractive index μ_i/μ_{i+1}

The orthogonal 3D-distance vector $\vec{\Delta_{xyz_{i,j}}}$ between the outgoing image ray and the approximate point coordinate is minimized (Rofallski and Luhmann, 2022):

$$\vec{\Delta_{xyz_{i,j}}} = \vec{P_j} - \vec{P_{o_{i,j}}} - \vec{A_n} \cdot \left(\frac{\vec{A_n} \cdot (\vec{P_j} - \vec{P_{o_{i,j}}})}{\left|\vec{A_n}\right|^2} \right) \quad (2)$$

$\vec{P_j}$ j^{th} point in object space

$\vec{P_{o_{i,j}}}$ Starting point of the outgoing ray for point j and exterior orientation i

$\vec{A_n}$ Direction vector of outgoing ray

The optimization approach is proven to provide comparable results to other strict approaches while requiring a fraction of computation time (Rofallski and Luhmann, 2022).

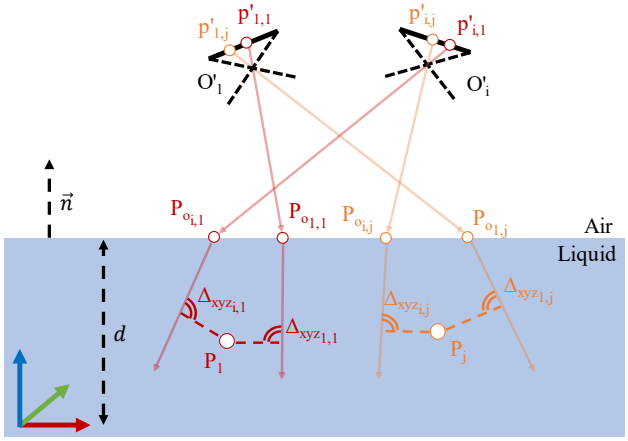

Figure 5. Ray tracing through object invariant refractive interface. The distance between the refracted ray and the object point is minimized for each observation. Additional refraction parameters are the refractive index of the liquid and position and orientation of the water surface, represented by $\vec{n}$ and d.

3.5 Scale calibration

With the gears used, the distance traveled per revolution can be obtained from the data sheets. Thus, each stepper motor position can be translated to a position on the respective axis. However, small production deviations or imperfections on the timing belt installation may affect the actual distance traveled. To obtain an accurate estimate, a FARO Vantage laser tracker was set up and a 1.5 inch Spherically Mounted Retroreflector (SMR) attached to the system (Figure 6). We then performed a calibration routine, consisting of 6 × 6 positions over the entire conservation tank (1170 mm (x) and 5000 mm (y)). The relation of the measured laser tracker coordinates to the calculated motor positions resulted in scale factors for x- and y-axis, individually. Table 1 shows the mean values for all 12 distances and the resulting scale factors.

Figure 6. Laser tracker (left foreground) measuring the SMR, attached to the measurement unit (red rectangle)

The data shows that the system had a repeatability of about 0.3 mm over distances of 5 m. The calibrated scale factors suggest an increase of distances along the x-axis of 0.56 mm/m and a decrease of distances along the y-axis of 1.03 mm/m. The distances were used in the following for constraints on projection centers.

Table 1. Results of the scale calibration for both axes. Calculated distance results from values provided by the motor steps with the nominal gear circumference; mean and standard deviation of measured distances result from laser tracker values.

Axis	Calc dist [mm]	Mean meas. dist. [mm]	Std. meas. dist [mm]	Calib. scale factor
x	1171.00	1171.65	0.28	1.00056
y	5000.00	4994.85	0.34	0.99897

4. Investigation on data modeling

In this section, we focus on the data from one measurement series, perform bundle adjustment with refraction correction and show influences of different scale definitions. We considered the data with the given parameters from Table 2. For reference, Table 3 provides information on the naming schema for the variants in the results section. For example, the analysis ”RTO_2S_0E_RO_free” was analyzed with the RTO approach, two scale bars, no exterior orientation constraints and a relative orientation constraint with simultaneously adjusted parameters.

The aim was to assess both refraction modeling effects and the choice of an appropriate scale definition with the given system configuration. Hence, we first provided an evaluation of a standard self-calibration approach, compared to a strict ray tracing approach, considering refractive effects of multimedia geometry. Further on, different scale definitions for the bundle were considered with this aerial-triangulation-like bundle.

Table 2. Parameters for the evaluated data set

Total (oriented) no. images	908 (893)
No. object points	594
No. image points	29587
Pixel size	4.8 µm
Stereo baseline	262 mm
Convergence angle	24.5°
Scale bars (longitudinal)	1 × 2 m
Scale bars (lateral)	2 × 1 m

Table 3. Notation for the different evaluated configurations

Calibration setup	
BRN	Brown model with radial-symmetric and tangential-asymmetric distortion and affinity and shear parameters. All parameters are adjusted.
RTO	Ray tracing in object space, according to Rofallski and Luhmann (2022) with IOP according to Brown. Only refractive index and interface position, orientation are adjusted
XS	Number of scale bars introduced to the bundle
XE	Number of scales between projection centers introduced to the bundle
RO_X	Relative orientation constraints, either with **fixed** or **free** values (simultaneously adjusted)

4.1 Multimedia effects

4.1.1 Standard calibrations We investigated the behavior of neglecting multimedia effects on the bundle geometry. First, we analyzed the data with a standard self-calibration bundle, including the model according to Brown (1971), as would be the case in air. Secondly, a pre-calibrated interior orientation with the applied Ray Tracing in Object Space (RTO) approach by Rofallski and Luhmann (2022) was performed. Here, and in all subsequent investigations, the interior orientation was held constant. Hence, apart from exterior orientations and object coordinates, only refractive parameters, i.e. orientation and position of the liquid surface and the refractive index of the liquid, were estimated. For scale definition the central long scale bar of approximately 2 m length was used. The other two scale bars of approximately 1 m length provided independent length measurement errors (LME), according to VDI/VDE 2634-1 (VDI/VDE-Gesellschaft Mess- und Automatisierungstechnik, 2002). The resulting data is shown in Figure 8 and corresponding statistics are presented in Table 4.

The Brown model lead to obvious distortions, visible both in 3D and in the statistics. In the 3D data, a banana-shaped curving of the entire object space was present with the Brown model which disappeared with the ray tracing approach. Overall accuracy was improved significantly from a relative accuracy of 1:127 up to 1:1500. The σ_0 value for the Brown model translates to $0.52\,\mathrm{px}$ whereas the respective value for RTO provided an estimate of accuracy in object space, despite no direct interpretation is known, so far (Rofallski and Luhmann, 2022). The refraction parameters were calculated significantly and provide plausible values.

Table 4. Results of multimedia effects investigation. Bracketed σ_0 value for RTO depicts standard deviation in object space. LME are length measurement errors for two independent scales. RA is relative accuracy, d is the distance from the projection center to the interface, μ_{liquid} is refractive index of the liquid. Bracketed values below depict 1σ standard deviation of estimated parameter. BRN Reverse refers to investigation in Section 4.1.2

	σ_0 [µm]	LME_1 [mm]	LME_2 [mm]	RA [1 : N]	d [mm]	μ_{liquid}
BRN	2.51	7.48	5.17	127	-	-
RTO	- (34.83)	0.21	-0.63	1500	235.60 (0.08)	1.3354 (2.6E-4)
BRN Reverse	3.37	0.09	0.80	1178	-	-

4.1.2 Reverse calibration To better understand the origin of the banana-shaped curve, we did a second analysis on the dataset, called ”reverse calibration”. Here, we performed bundle adjustment with the same observations twice. In the first run, we used the object points from the RTO dataset and introduced these as errorless ground control points to calibrate the camera with the Brown model. In the second run, the calibrated interior orientation was introduced to the bundle as fixed parameters and ran the same bundle adjustment with free object points and exterior orientations. This way, the factor of self-calibration was eliminated from the adjustment without actually performing it in the medium. The last row of Table 4 provides statistics to this approach, Figure 7 shows the differences between the parameters from self-calibration and the parameters from this approach.

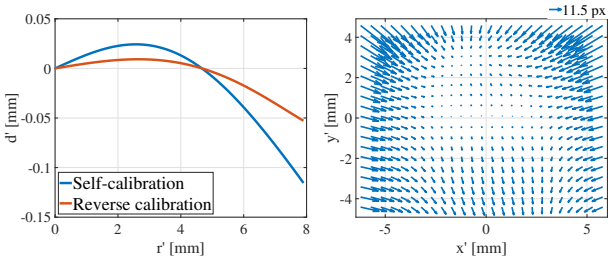

(a) Radial-symmetric coefficients (b) Difference of distortions

Figure 7. Distortion of self-calibrated and reverse calibrated interior orientation with Brown model

Despite the increased standard deviation of unit weight ($0.70\,\mathrm{px}$), this adjustment strategy provided a substantial improvement and a similar geometry to the RTO approach. LME and RA were slightly inferior compared to the RTO approach but were on the order of submillimeter accuracy, just as the physically strict modeling. However, these results can only be generated based on the computed object points from the ray tracing approach and cannot reliably provide better results. Hence, in the following, we refrain from considering the Brown approach further and only focus on the RTO algorithm.

4.2 Scale definition

4.2.1 Experimental design The challenging bundle geometry requires an appropriate scale definition to obtain reliable and accurate results. We investigated three possible definitions and evaluated their influences on the bundle solution.

1. Submerged CFK scale bars
2. Relative orientation constraints of the stereo system
3. Distance constraints between exterior orientations, provided by the biaxial measurement system

All investigated options were set as a minimum configuration, meaning that only one necessary constraint was introduced to the bundle adjustment at a time to remain a free net adjustment. This could either be scale constraints from scale bars, respectively, exterior orientations or a fixed relative orientation.

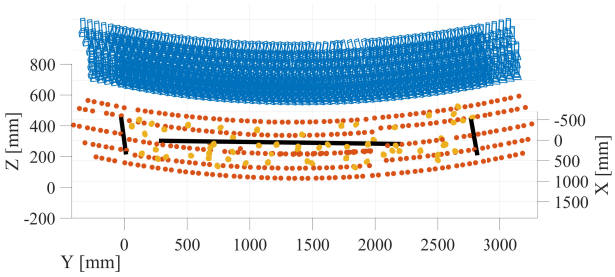

(a) Brown

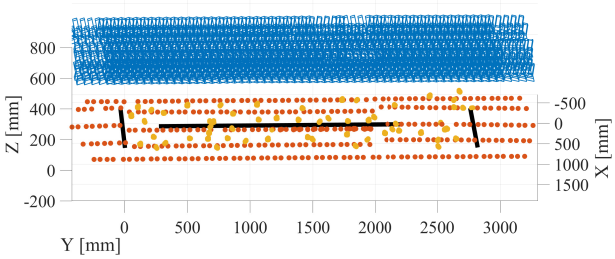

(b) Ray Tracing in Object Space (RTO)

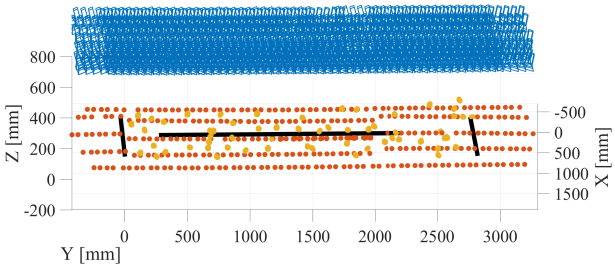

(c) Brown - reverse calibration

Figure 8. Geometry for Brown model with self-calibration (a), physically modeled Ray Tracing in Object Space with pre-calibrated interior orientation (b) and reverse calibrated Brown model (c). Black: Scale bars; Blue: Camera stations; Red: Datum points; Yellow: Marker (deformation) points

Furthermore, we examined the possibility of introducing a relative orientation constraint without predetermined values. This approach does not impose scale constraints on the bundle but may enhance geometric stability.

The submerged CFK scale bars provided accurate length information in object space. The determined lengths were accurate to $0.02\,\mathrm{mm}$, providing a superior scale information. We considered both a single scale and a dual scale variant where we either only introduced the longest scale along the y-axis or also added a second shorter scale along the x-axis for the dual scale variant.

The stereo system sat on a fixed base, hence allowing relative orientation to be assumed constant. In a calibration in air, the values of relative orientation were obtained by self-calibration beforehand. We both investigated the introduction of fixed, errorless Lagrangian constraints and as free constraints without providing fixed values to the system of normal equations.

Whereas the former two options are well-known from multi-image and stereo photogrammetry, the third option specifically arose from the possibilities of the developed measurement system. The calibrated circumference of the gears and the repeatability provided possible scale between all exterior orientations. The determined precision of approximately $0.3\,\mathrm{mm}$ from Section 3.5 implies that this accuracy may not be as high as the scales which were determined with accuracy of $0.02\,\mathrm{mm}$ but the calibrated distances were longer and more constraints, theoretically all combinations, were possible. This raises the general question regarding the length, distribution and quality of used scales in a bundle, like in Reznicek et al. (2016) which is not within the scope of this paper. Hence, we only investigated comparable amounts to the scale bar definitions (one or two constraints).

4.2.2 Results Relevant statistics are presented in Table 5. The relative accuracy (RA) was calculated as the ratio of the worst LME to its corresponding nominal length (Luhmann et al., 2020). Generally, an accuracy gain with introduction of more constraints was visible. Especially, relative orientation constraints improve relative accuracy substantially. The second major accuracy gain resulted from the introduction of more scale constraints. This particularly shows for scale bars but can only partly be seen for the projection centers. Only the combined introduction of a free relative orientation with two constraints between projection centers lead to an improvement compared to the same analysis with only one scale constraint. However, accuracy was generally higher with an introduction of scale bars, rather than constraints between exterior orientations. The derived distance d ranged between 235 and $239\,\mathrm{mm}$, depending on the type of analysis performed. Generally, comparable parameters for both d and μ_{water} resulted from similar analyses. This means that for example a free relative orientation with one scale bar produced similar results, independent of the scale definition through projection centers or a scale bar. The same applied to a single scale without relative orientation constraints, just as for the same analysis with two scale definitions.

Nominally, the highest accuracy resulted from the combination of free relative orientation and two scale bars included. For LME comparison, only one scale bar was available as the other two were included as system scales into the adjustment and thus do not provide independent lengths. The deviation of these two system scales was $\pm 0.07\,\mathrm{mm}$, still showing indication of high precision. Better verification could be performed on the data that included scales from relative or exterior orientation. Here, the variant with free relative orientation and two scales between projection centers provided comparable LME values of less than $0.1\,\mathrm{mm}$.

4.3 Discussion

A major accuracy loss from performing self-calibration with the Brown model was first shown in the multimedia evaluation. This could have resulted from both the negligence of refraction and the error-prone self-calibration in this bundle geometry where no images from a further distance could be acquired to stabilize the geometry. Hence, the banana-shaped curve may have resulted from a combination of the two factors. Calibrating in the liquid would whirl up the liquid and hence distort the plane character of the surface and also require to work in the conservation liquid. Both factors complicate a proper pre-calibration with multimedia effects to an impractical degree, thus requiring the application to employ a strict ray tracing approach. Since self-calibration combined with refraction calibration is highly correlated, a camera pre-calibration is always recommended to obtain reliable and uncorrelated results. We have shown that, with a good calibration, also the Brown model may provide comparable

Table 5. Results for varying bundle adjustment constraints. Value description is identical to Table 4. Bold entries have lowest standard deviation, lowest LME or highest RA per column and data set.

		σ_0 [µm]	LME_1 [mm]	LME_2 [mm]	RA $[1:N]$	d [mm]	μ_{liquid}
Single scale	RTO_1S_0E	**- (34.82)**	0.21	-0.63	1500	235.54 (0.08)	1.3354 (2.6E-4)
	RTO_1S_0E_RO_free	- (36.78)	**-0.04**	**-0.11**	**8675**	**235.27 (0.05)**	**1.3334 (2.4E-4)**
	RTO_0S_1E	**- (34.82)**	0.25	-0.58	1627	235.60 (0.08)	1.3354 (2.6E-4)
	RTO_0S_1E_RO_free	- (36.79)	0.31	0.24	3038	**235.37 (0.05)**	**1.3334 (2.4E-4)**
	RTO_0S_0E_RO_fixed	- (228.28)	0.13	**0.02**	7523	239.04 (0.32)	1.3269 (1.4E-3)
Dual scale	RTO_2S_0E	- (34.80)	0.40	-	2373	239.21 (0.08)	1.3354 (2.6E-4)
	RTO_2S_0E_RO_free	- (36.76)	**0.00**	-	**1570113**	**238.84 (0.05)**	**1.3334 (2.4E-4)**
	RTO_0S_2E	**- (34.79)**	0.07	-0.75	1256	239.16 (0.08)	1.3354 (2.6E-4)
	RTO_0S_2E_RO_free	- (36.76)	0.06	**-0.01**	16163	**238.89 (0.05)**	**1.3334 (2.4E-4)**

results to the ray tracing approach. However, this approach requires a ray tracing adjustment to accurately calculate the object points, if no prior knowledge of the geometry is provided. The implicit Brown calibration through the liquid remains valid only as long as all related parameters remain stable, i.e. camera orientation to the liquid surface and its refractive index. Thus, it is not possible to calibrate the camera with this approach over a different tank with more favorable geometry or such. Hence, though achieving comparable results, a ray tracing approach was essential in this application.

Considering only refraction correction would have been sufficient to achieve submillimeter accuracy over distances of more than $2\,\mathrm{m}$. However, the achieved relative accuracy of 1:1500 still left room for improvement by exploiting other a-priori known constraints. Especially constraining relative orientation and including a second scale constraint resulted in a significantly higher overall precision and relative accuracy in object space. The fixed relative orientation provided good relative accuracy but resulted in a significantly higher standard deviation of unit weight. It was not clear why this resulted from the adjustment as the general accuracy is rather high and estimated relative orientations did not strongly deviate from the pre-calibrated values. The longer scale distances between projection centers did not provide a better scale definition than the CFK scale bars. This was probably caused by the lower accuracy compared to the highly accurate scale bars. Possibly, an increased coverage, providing longer scales between projection centers might improve the accuracy in the future.

5. Conclusion

In this contribution, we introduced a biaxial measurement unit to observe waterlogged wood in a conservation tank. The system is generally modular and may be applied to other applications with similar bundle geometries, as well. The system was scale-calibrated but already provided a repeatable precision of about $0.3\,\mathrm{mm}$ with a scale drift of $0.5\,‰$ and $1\,‰$ on the respective axes.

We furthermore adapted a fast ray tracing approach (RTO) to an object-invariant interface and included multi-camera systems with relative orientation. The performed evaluations on these parameters showed that in this application a ray tracing approach was imperative. Standard self-calibration failed completely with a resulting banana-shaped curve of object space. Employing a reverse calibration scheme, the results could be substantially improved but always requires knowledge of object points to obtain the necessary pre-calibrated interior orientation.

Inclusion of relative orientation showed the best results which will be performed in the future when deformation data will be analyzed from multiple epochs. It is generally evident that no standard bundle adjustment program could perform all these analyses (ray tracing, multi-camera constraints, projection center constraints), hence all aspects had to be provided by own implementations. For an automation of the adjustment process for each epoch, the bundle adjustment software was ported to a dynamic web application[3]. This will be tightly included in the future to further outsource the computation load to server-side performance architecture.

Adding a maximum of two exterior orientation constraints also helped improving the overall accuracy of the bundle. In addition, theoretically, every distance combination between projection centers could have been included in the adjustment. For a strict inclusion of all possible exterior orientation constraints, a 2D-Affine transformation with two fixed scales could be included. Affine transformation might be necessary, as the two axes of the unit are not guaranteed to be orthogonal which would have to be accounted for in this approach.

At this stage, the turbidity in the conservation liquid was low, providing very good image quality. This generally changes after some time when reactions of the conservation agent and the wood increase turbidity. For future work, a laser line was included to perform laser triangulation if turbidity increases heavily. The data is concurrently acquired but is yet to be analyzed.

[3] https://bundle.projekte.services.fbbgg.hs-woe.de

Acknowledgements

The authors want to express their gratitude to colleagues from Jade University, namely Nils Sander, Marco Wilmes and Holger Groenewold, for their invaluable help on the construction of the measurement unit. Thanks to the Agency of Cultural Heritage Protection of Lower-Saxony (NLD Hannover), particularly Dr. Marion Heumüller, the wood was stored and treated in stainless steel tanks on loan at Denkmal3D. Further thanks to the photogrammetry working group at IAPG for valuable feedback and discussion. Finally, the authors would like to thank the German Federal Foundation for the Environment (DBU), in particular Constanze Fuhrmann for their trust and funding OptiKons project (AZ 37885/01-45).

References

Agrawal, A., Ramalingam, S., Taguchi, Y., Chari, V., 2012. A theory of multi-layer flat refractive geometry. *IEEE Conf. Comput. Vis. and Pattern Recognit.*, 3346–3353.

Björdal, C. G., 2000. *Waterlogged archaelogical wood*. Acta Universitatis Agriculturae Sueciae. Silvestria, 142, Sveriges Lantbruksuniv, Uppsala.

Bratasz, Ł., Kozłowski, R., 2005. Laser Sensors for Continuous In-Situ Monitoring of the Dimensional Response of Wooden Objects. *Studies in Conservation*, 50(4), 307–315.

Broda, M., Hill, C. A. S., 2021. Conservation of Waterlogged Wood—Past, Present and Future Perspectives. *Forests*, 12(9), 1193.

Brown, D. C., 1971. Close-Range Camera Calibration. *Photogrammetric Engineering*, 37(8), 855–866.

Colson, A., 2024. *Spatial Monitoring of the Bremen Cog - Long-term Preservation of Archaeological Wooden Ships in Museums*. Schriften aus der Fakultät Geistes- und Kulturwissenschaften, 46, University of Bamberg Press.

Colson, A., Hastedt, H., Luhmann, T., Hess, M., 2022. The role of conservators in the implementation of surveying techniques: Reflections on the bremen cog monitoring project. *Wet Organic Archaeological Materials 2019*, 281–286.

Colson, A., Heumüller, M., Abbentheren, E., 2023. The Wooden Trackway PR6, Aschener Bog, Lower-Saxony, Germany. *ISPRS Annals of Photogrammetry, Remote Sensing and Spatial Information Sciences*, X-M-1-2023, 41–46.

Giachi, G., Capretti, C., Macchioni, N., Pizzo, B., Donato, I. D., 2010. A methodological approach in the evaluation of the efficacy of treatments for the dimensional stabilisation of waterlogged archaeological wood. *Journal of Cultural Heritage*, 11(1), 91–101.

Glassner, A. S. (ed.), 1989. *An introduction to ray tracing*. Acad. Press, London.

Hastedt, H., Luhmann, T., Colson, A., 2019. Large-volume photogrammetric deformation monitoring of the bremen cog. *Proceedings from the 4th Joint International Symposium on Deformation Monitoring*.

Hauer, D., Colson, A., Hastedt, H., Gamstedt, K., 2022. Monitoring structural change of large, complex archaeological wooden objects: Application of fixed target photogrammetry. *Wet Organic Archaeological Materials 2019*, 287–296.

Jensen, P., Gregory, D. J., 2006. Selected physical parameters to characterize the state of preservation of waterlogged archaeological wood: a practical guide for their determination. *Journal of Archaeological Science*, 33(4), 551–559.

Jordt-Sedlazeck, A., Koch, R., 2012. Refractive calibration of underwater cameras. Fitzgibbon A., Lazebnik S., Perona P., Sato Y., Schmid C. (eds), *Computer Vision – ECCV 2012*, Lecture Notes in Computer Science, 7576, Springer, Berlin, Heidelberg, 846–859.

Kotowski, R., 1988. Phototriangulation in Multi-Media Photogrammetry. *International Archives of Photogrammetry and Remote Sensing*, 324–334.

Luhmann, T., Robson, S., Kyle, S., Boehm, J., 2020. *Close-range photogrammetry and 3D imaging*. 3rd edition edn, De Gruyter, Berlin, Boston.

Mulsow, C., 2010. A flexible multi-media bundle approach. *ISPRS - International Archives of the Photogrammetry, Remote Sensing and Spatial Information Sciences*, XXXVIII/5, 472–477.

Mulsow, C., Maas, H.-G., 2014. A universal approach for geometric modelling in underwater stereo image processing. *2014 ICPR Workshop on Computer Vision for Analysis of Underwater Imagery (CVAUI)*, 49–56.

Reznicek, J., Hastedt, H., Ekkel, T., Luhmann, T., Jepping, C., 2016. Analysen zur Datumsfestlegung in photogrammetrischen Projekten großer Volumina. *Publikationen der DGPF, Band 25*, 259–270.

Robson, S., Bucklow, S., Woodhouse, N., Papadaki, H., 2004. Periodic Photogrammetric Monitoring and Surface Reconstruction of a Historical Wood Panel Painting for Restauration Purposes. *ISPRS - International Archives of the Photogrammetry, Remote Sensing and Spatial Information Sciences*, 395–400.

Rofallski, R., Luhmann, T., 2022. An Efficient Solution to Ray Tracing Problems in Multimedia Photogrammetry for Flat Refractive Interfaces. *PFG – Journal of Photogrammetry, Remote Sensing and Geoinformation Science*.

Stelzner, J., Stelzner, I., Martinez-Garcia, J., Gwerder, D., Wittköpper, M., Muskalla, W., Cramer, A., Heinz, G., Egg, M., Schuetz, P., 2022. Stabilisation of waterlogged archaeological wood: the application of structured-light 3D scanning and micro computed tomography for analysing dimensional changes. *Heritage Science*, 10(1), 60.

Treibitz, T., Schechner, Y., Kunz, C., Singh, H., 2012. Flat Refractive Geometry. *IEEE transactions on pattern analysis and machine intelligence*, 34(1), 51–65.

van Dijk, N. P., Gamstedt, E. K., Bjurhager, I., 2016. Monitoring archaeological wooden structures: Non-contact measurement systems and interpretation as average strain fields. *Journal of Cultural Heritage*, 17, 102–113.

VDI/VDE-Gesellschaft Mess- und Automatisierungstechnik, 2002. *VDI/VDE 2634 Blatt 1: Optische 3-D-Messsysteme - Bildgebende Systeme mit punktförmiger Antastung*. Beuth Verlag GmbH.

Viñas, S. M., 2002. Contemporary theory of conservation. *Studies in Conservation*, 47(Supplement-1), 25–34.